LETTER

https://doi.org/10.1038/s41586-019-1239-7

Lattice anchoring stabilizes solution-processed semiconductors

Mengxia Liu[1], Yuelang Chen[2], Chih-Shan Tan[1], Rafael Quintero-Bermudez[1], Andrew H. Proppe[1,2], Rahim Munir[3,4], Hairen Tan[1,5], Oleksandr Voznyy[1], Benjamin Scheffel[1], Grant Walters[1], Andrew Pak Tao Kam[1], Bin Sun[1], Min-Jae Choi[1], Sjoerd Hoogland[1], Aram Amassian[3,6], Shana O. Kelley[2,7], F. Pelayo García de Arquer[1] & Edward H. Sargent[1]*

The stability of solution-processed semiconductors remains an important area for improvement on their path to wider deployment. Inorganic caesium lead halide perovskites have a bandgap well suited to tandem solar cells[1] but suffer from an undesired phase transition near room temperature[2]. Colloidal quantum dots (CQDs) are structurally robust materials prized for their size-tunable bandgap[3]; however, they also require further advances in stability because they are prone to aggregation and surface oxidization at high temperatures as a consequence of incomplete surface passivation[4,5]. Here we report 'lattice-anchored' hybrid materials that combine caesium lead halide perovskites with lead chalcogenide CQDs, in which lattice matching between the two materials contributes to a stability exceeding that of the constituents. We find that CQDs keep the perovskite in its desired cubic phase, suppressing the transition to the undesired lattice-mismatched phases. The stability of the CQD-anchored perovskite in air is enhanced by an order of magnitude compared with pristine perovskite, and the material remains stable for more than six months at ambient conditions (25 degrees Celsius and about 30 per cent humidity) and more than five hours at 200 degrees Celsius. The perovskite prevents oxidation of the CQD surfaces and reduces the agglomeration of the nanoparticles at 100 degrees Celsius by a factor of five compared with CQD controls. The matrix-protected CQDs show a photoluminescence quantum efficiency of 30 per cent for a CQD solid emitting at infrared wavelengths. The lattice-anchored CQD:perovskite solid exhibits a doubling in charge carrier mobility as a result of a reduced energy barrier for carrier hopping compared with the pure CQD solid. These benefits have potential uses in solution-processed optoelectronic devices.

Solution-processed semiconductors combine ease of processing, scalable fabrication and compatibility with flexible substrates—compelling properties for next-generation optoelectronic devices[6]. Given the steadily increasing performance of solution-processed materials in sensing[7], light-emission[8,9] and photovoltaics[3,10], their limited stability is an urgent challenge. Much progress has been made towards the goal of long-term stability in printable semiconductors[11,12], but their lifetime in ambient room conditions and at elevated temperatures and humidity has not yet fulfilled the stringent requirement of multi-thousand hours for industrial applications.

Hybrid organic–inorganic perovskites (solution-processed, structurally soft materials[13]) have attracted intense interest because of their remarkable photovoltaic performance[14]. The best certified power conversion efficiency (PCE) of perovskite solar cells has rapidly advanced to 23.7%[15]. However, the limited environmental and thermal stability of perovskites threatens to hamper their widespread deployment in optoelectronics and energy harvesting. This instability stems from the volatility of the perovskites' organic components, aggravated by external stress such as heat and light[16].

These issues can potentially be addressed using all-inorganic perovskites, of which caesium lead halide perovskite, $CsPbX_3$ (X = halide), is a candidate of interest. Cubic-phase (α-phase) $CsPbI_3$ has a bandgap suited to tandem solar cells[1]. Unfortunately, it transforms readily into the transparent phase (δ-phase) under ambient conditions at room temperature[2], because of the low formation energy of the δ-phase at room temperature and the high flexibility of the perovskite lattice[17]. Substituting part of the iodine with bromine improves the stability of the α-phase; however, mixed-halide perovskites undergo phase segregation when annealed at high temperature in ambient air. Stabilizing the α-phase $CsPbX_3$ perovskite is of urgent interest.

CQDs, also solution-processed and widely studied for optoelectronic applications, have a bandgap that can be tuned by means of the quantum size effect across the wide solar spectrum[3]. Advanced materials processing strategies and device architectures have contributed to improved solar cell performance[10,11]; however, incomplete surface passivation leads to CQD aggregation and surface oxidation[4], particularly when operated at high temperatures. These militate against device performance and lifetime.

Previously investigated methods to improve the stability of inorganic solution-processed materials have advanced each material system considerably. For α-phase $CsPbX_3$ perovskites, decreasing grain size or adding dopants proved useful for phase stabilization[2,18–20]. However, the stability is still not satisfactory and a large number of surface trap states are detrimental to their electronic properties[21]. Moreover, stability under demanding accelerated lifetime testing (that is, exposing it to conditions that cause faster degradation), such as at high temperatures in air, remains to be addressed.

For CQDs, improved air stability has been achieved using strongly bound surface ligands[3,11]. Unfortunately, the oxidation of sulfur-rich facets in lead sulfide CQDs occurs at temperatures as low as 50 °C and causes the device performance to deteriorate[5,22]. A monolayer of perovskite provided surface passivation of CQDs, a promising insight on the path to longer-term stability[23–26]; however, these perovskites failed to prevent oxidation and aggregation of the CQDs at high temperatures. In sum, ever more effective stabilization strategies are needed in both perovskites and CQDs.

We sought an approach that would block the phase transition of $CsPbX_3$. Our aim was to prevent atomic site adjustment and lattice deformation by incorporating inclusions—CQDs—that were lattice-matched to the desired, but otherwise unstable, α-solid, while being appreciably mismatched with the δ-phase.

The new hybrid material is more stable than either component. CQDs promote the epitaxial growth of α-phase perovskite and anchor the atoms of the perovskite to the CQD surfaces. This leads to improved ambient lifetime, which reaches more than 6 months for the newly stabilized $CsPbX_3$ perovskite. It also leads to largely enhanced

[1]Department of Electrical and Computer Engineering, University of Toronto, Toronto, Ontario, Canada. [2]Department of Chemistry, University of Toronto, Toronto, Ontario, Canada. [3]KAUST Solar Center (KSC) and Physical Sciences and Engineering Division, King Abdullah University of Science and Technology, Thuwal, Saudi Arabia. [4]Helmholtz-Zentrum Berlin für Materialien und Energie, Berlin, Germany. [5]National Laboratory of Solid State Microstructures, Jiangsu Key Laboratory of Artificial Functional Materials, College of Engineering and Applied Sciences, Nanjing University, Nanjing, China. [6]Department of Materials Science and Engineering, North Carolina State University, Raleigh, NC, USA. [7]Department of Pharmaceutical Sciences, Leslie Dan Faculty of Pharmacy, University of Toronto, Toronto, Ontario, Canada. *e-mail: ted.sargent@utoronto.ca

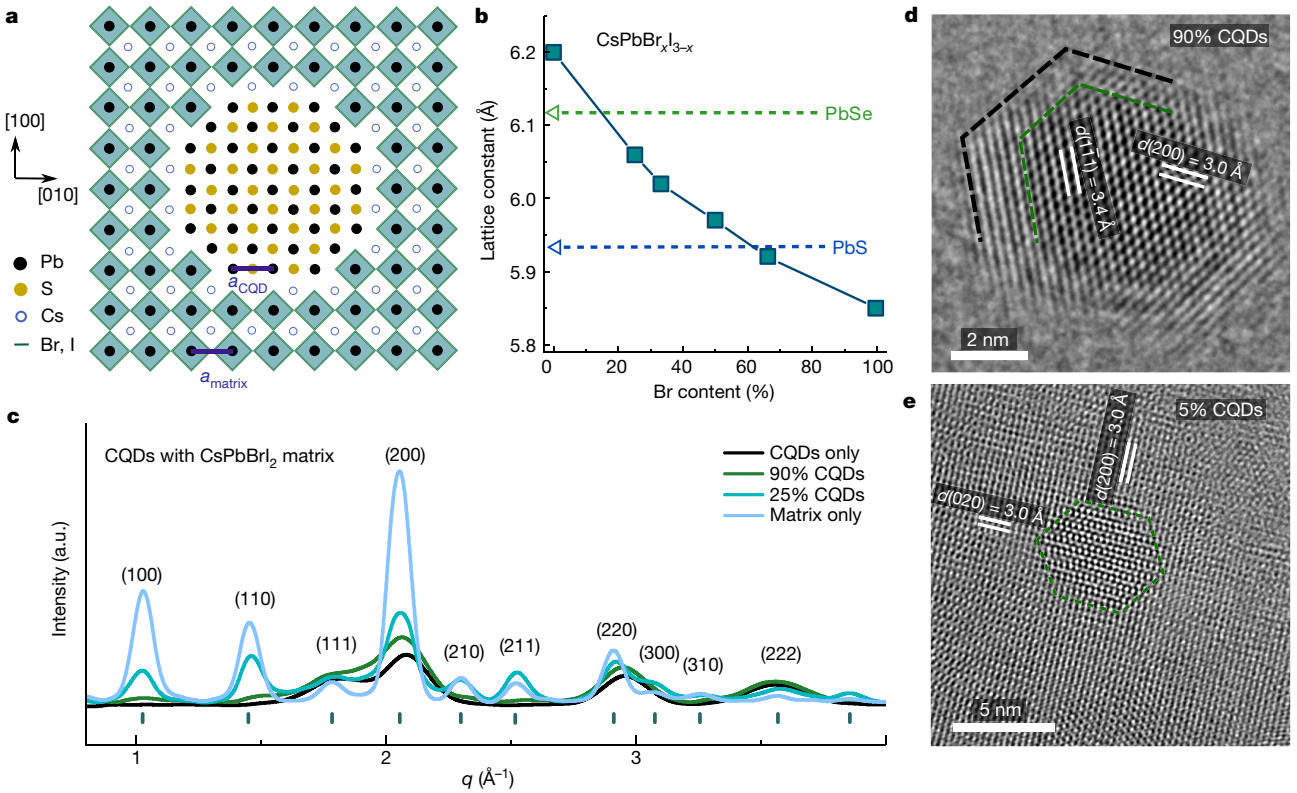

Fig. 1 | Epitaxial alignment between caesium lead halide perovskite and CQDs. a, Schematic depiction of the atomistic model of a CQD:perovskite lattice-anchored hybrid materials system. **b**, The lattice constant of lead chalcogenide CQDs and caesium lead halide perovskites of different stoichiometry. **c**, Synchrotron X-ray diffraction measurements of the CQDs with a perovskite matrix, showing the successful incorporation of the CQD and perovskite components in the hybrid materials. **d**, **e**, HRTEM images of the lattice-anchored CQD:perovskite hybrid materials at high (**d**) and low (**e**) CQD concentration. The shell has a lower contrast compared with the CQDs, as the perovskite has a lower density than PbS. These results confirm the crystal structure and demonstrate the epitaxial orientational alignment at different facets.

thermal stability in air: materials do not degrade following exposure to 200 °C for 5 h. This is an order of magnitude longer than for the pure perovskite absent the CQDs.

The lattice-anchored hybrid materials system is depicted in Fig. 1a. Lead chalcogenides (PbS and PbSe) with their rock salt structure have a Pb–Pb distance of 5.94 Å and 6.12 Å (ref. [27]), respectively, close to that of the α-phase $CsPbBr_xI_{3-x}$ perovskite (5.85 Å to 6.21 Å)[1]. By tuning the ratio of Br to I in the matrix composition, we achieve near-zero lattice mismatch (ε) for PbS CQDs at a Br content of approximately 66% ($\varepsilon < 0.2\%$), enabling the strain-free epitaxial growth of perovskite (Fig. 1b).

We prepared the hybrid films using $CsPbBr_xI_{3-x}$ matrix solutions combined with pre-exchanged CQDs (Extended Data Fig. 1). By controlling the weight ratio of CQD to perovskite, we tuned the amount of perovskite matrix and the expected average dot-to-dot distance[24]. The hybrid ink was deposited by spin-coating to achieve an optimized thickness, followed by an annealing process to crystallize the matrix and remove solvent residue. Elemental mapping from energy dispersive X-ray spectroscopy (EDX) in scanning electron microscopy (SEM) indicates a uniform elemental distribution in the hybrid films (Extended Data Fig. 2).

We carried out synchrotron high-resolution X-ray diffraction (XRD) measurements to elucidate the composition and crystal structure of the hybrid films (Fig. 1c, Extended Data Fig. 3). In this measurement, we used films with CQDs in a matrix of either $CsPbBrI_2$ or $CsPbBr_2I$. XRD demonstrates that as-synthesized perovskite and CQDs are each in the cubic phase: $CsPbBrI_2$ shows a 1% lattice mismatch with PbS CQDs; in contrast, $CsPbBr_2I$ and PbS show complete agreement in lattice planes (Extended Data Fig. 3b).

We then used high-resolution transmission electron microscopy (HRTEM) to ascertain further the crystal structure and identify the orientation of perovskites and CQDs relative to one another (Fig. 1d, e; Extended Data Fig. 4a, b). The real-space images show that a perovskite shell forms at high CQD concentration and inherits the crystalline orientation of its associated dot (Fig. 1d). No spacing differences between core CQD and perovskite shell were observed from HRTEM images, indicating epitaxial orientational alignment at two dominant facets. Lattice fringes of 3.4 ± 0.1 Å and 3.0 ± 0.1 Å spacing are ascribed to (1$\bar{1}$1) and (200) planes, respectively, both for the CQDs and for the matrix. The fast Fourier transform image also confirms the lattice matching between two constituent materials (Extended Data Fig. 4a, b). As the amount of perovskite increases, the shell grows thicker and forms a continuous matrix with dots embedded inside (Fig. 1e). The incorporation of CQDs is further confirmed by elemental distribution analysis using electron energy-loss spectroscopy (EELS) mapping (Extended Data Fig. 4c, d).

We then investigated the effect of embedded dots on perovskite lifetime. In pristine $CsPbBr_xI_{3-x}$ films, phase transition and phase segregation are detrimental to their stability. An α-phase (dark) to δ-phase (transparent) transition occurs, particularly in films with low Br content, at low temperatures (for example room temperature), leading to a loss in the amplitude of film absorption. Phase segregation occurs when mixed-halide perovskite films are annealed in air at high temperatures, a result of the increased ion migration triggered by oxygen and heat. This results in separated Br-rich phases and I-rich phases (Fig. 2a), leading to a blueshift in the absorption edge. Film degradation is thus readily witnessed through the changes in absorbance and shift in absorption edge (Fig. 2b).

We used a volume fraction of CQDs below 15% to ensure uniform coverage and maintain the original grain size of perovskites (Extended Data Fig. 1c–f). The films were stored in air at room ambient conditions, under 30% ± 5% relative humidity at 25 °C, unencapsulated (that is, without sealing or protection from air). Our findings show that the incorporation of CQDs improves the stability of perovskite films

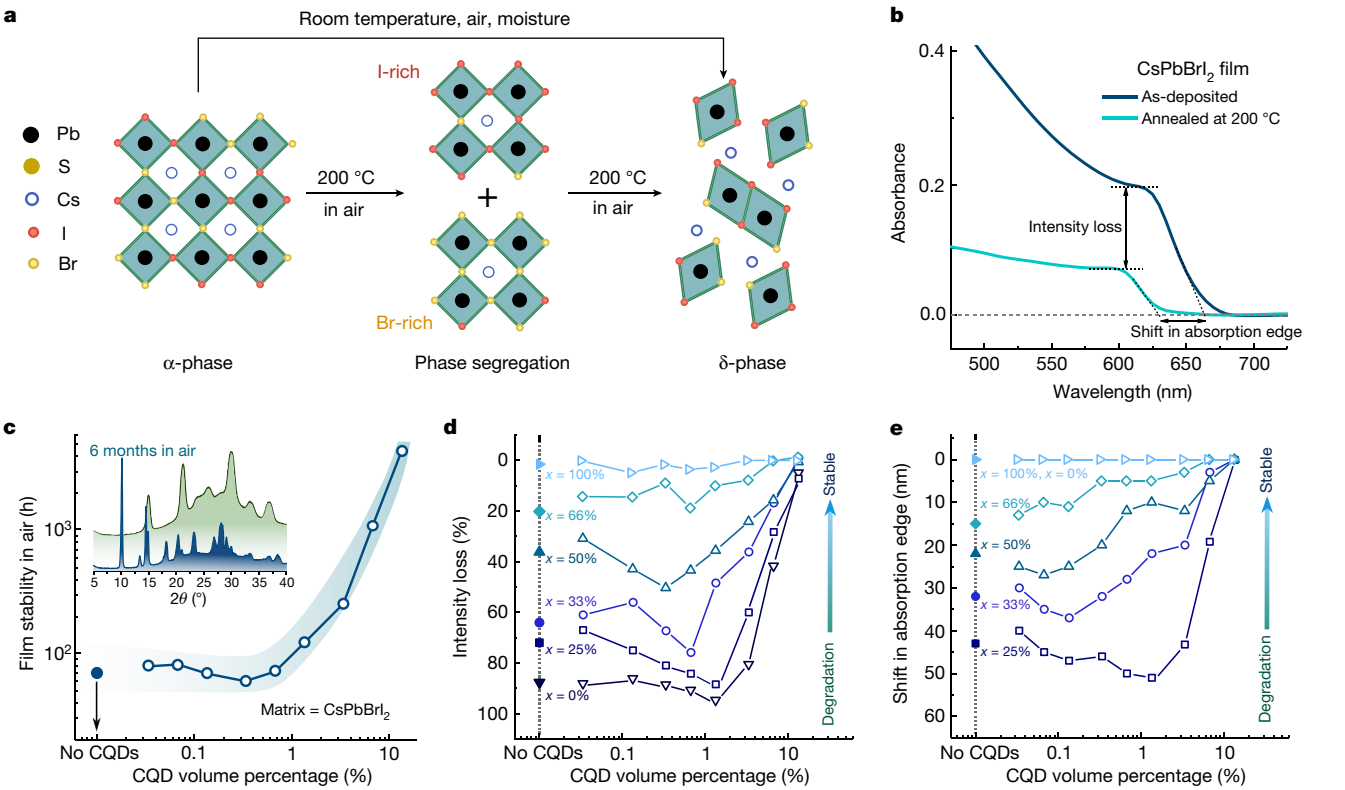

Fig. 2 | Stability of CQD-anchored caesium lead halide perovskites. **a**, Schematic of phase transition and separation in caesium lead halide perovskites. The transition from α-phase to δ-phase occurs at room temperature on exposure to moisture and air. Mixed halide perovskite samples, when heated to a high temperature in air, segregate into Br-rich and I-rich phases. **b**, The absorption spectra of pristine $CsPbBrI_2$ film before and after annealing at 200 °C for 5 h. The high annealing temperature leads to a notable phase degradation and segregation, which is verified by the changes in absorbance and the shift of the absorption edge, respectively. **c**, Stability of the lattice-anchored $CsPbBrI_2$ perovskite with different ratios of CQDs. The film stability is improved from three days to more than six months when 13 vol% CQDs are incorporated. Inset, X-ray diffraction of $CsPbBrI_2$ films with 13 vol% CQDs (green trace) and without CQDs (blue trace) after being stored in air for 6 months. **d**, **e**, The intensity loss in absorbance (**d**) and the shift in the absorption edge (**e**) after 5 h of annealing in air. *x* is the Br content.

by an order of magnitude (Extended Data Fig. 5a). We associate the improved stability with the high formation energy of the α/δ-phase interface. For $CsPbBrI_2$ perovskite, room-ambient stability is enhanced from 3 days to more than 6 months when 13 vol% CQDs are incorporated (Fig. 2c). XRD measurements confirm that the crystal structure remains unchanged after 6 months' storage. This strategy is compatible with previously reported methods[2] and allows for more than 6 months' stability in lattice-anchored $CsPbI_3$ (Extended Data Fig. 5b).

We then explored the thermal stability of perovskites in air. The absorption spectra of films were recorded before and after annealing in air at 200 °C for 5 h (Fig. 2d, e). Phase segregation occurs in pristine perovskite films within 30 min. However, this is largely suppressed when CQDs are integrated at a concentration above 6%: no film degradation is observed following 5 h of annealing in air.

We found the extent of improvement in film stability to depend strongly on the lattice mismatch between CQDs and perovskite. For CQD:$CsPbBr_2I$ samples in which near zero lattice mismatch is achieved, reduced intensity loss in absorbance and less shift in absorption edge are detected with increasing CQD concentrations, showing a gradual improvement in film stability. When lattice mismatch increases as we decrease the Br content, a larger strain is generated at interfaces. The stability as a function of increasing CQD concentration follows a V-shaped trend, first declining and then improving. We explain this by invoking interfacial strain between perovskites and CQDs: an unstrained CQD/perovskite interface is the most energetically favourable, and a certain amount of elastic strain can be accommodated without generating dislocations or defects[28]. In a lattice-mismatched system, a lower CQD concentration results in more perovskite layers between neighbouring CQDs and consequently increases the effects of strain. At low CQD loading, the interfacial strain is large enough to generate atomic dislocations. In this case, CQD surfaces act as defect centres, and the increasing concentration thus leads to a decreased lifetime of the perovskite. When the dot-to-dot distance is small enough to keep the strain energy below the formation energy of dislocations[29], the stability is increased. As a result, a perovskite matrix with the larger lattice mismatch demands a higher CQD concentration to anchor the atoms and achieve improved lifetime (Fig. 2d, e). This result is consistent with the observed phase stability measured at room temperature (Extended Data Fig. 5a).

We then investigated the thermal stability of CQDs when a perovskite matrix is added. Our hypothesis was that passivation provided by the perovskite matrix could inhibit oxidation and aggregation of CQDs.

We carried out in situ grazing-incidence small-angle X-ray scattering (GISAXS) measurements to track changes in CQD packing density and uniformity at elevated temperatures (Fig. 3). Before annealing, pure and hybrid films each present a hexagonal diffraction pattern, indicating an orientational ordering of CQDs (Extended Data Fig. 6). Azimuthal integration of the diffraction pattern (Fig. 3c, d) reveals changes at elevated temperatures: pure CQD films begin to show aggregation at relatively low temperatures (40 °C) and lose packing uniformity rapidly as temperature increases. By contrast, no degradation is observed below 100 °C in the matrix-protected films. Following annealing, the hexagonal pattern is no longer observable in pure CQD films; whereas it is sustained in hybrid films (Fig. 3a, b).

Photoluminescence (PL) studies affirm this finding: we recorded the PL intensity of films following annealing under 100 °C for different periods of time (Fig. 3e). The pure CQD film shows a rapid PL quenching and loses half of the intensity after an hour, which is consistent with a previous report[5]. In contrast, matrix-protected films maintain 90% of the initial value following annealing.

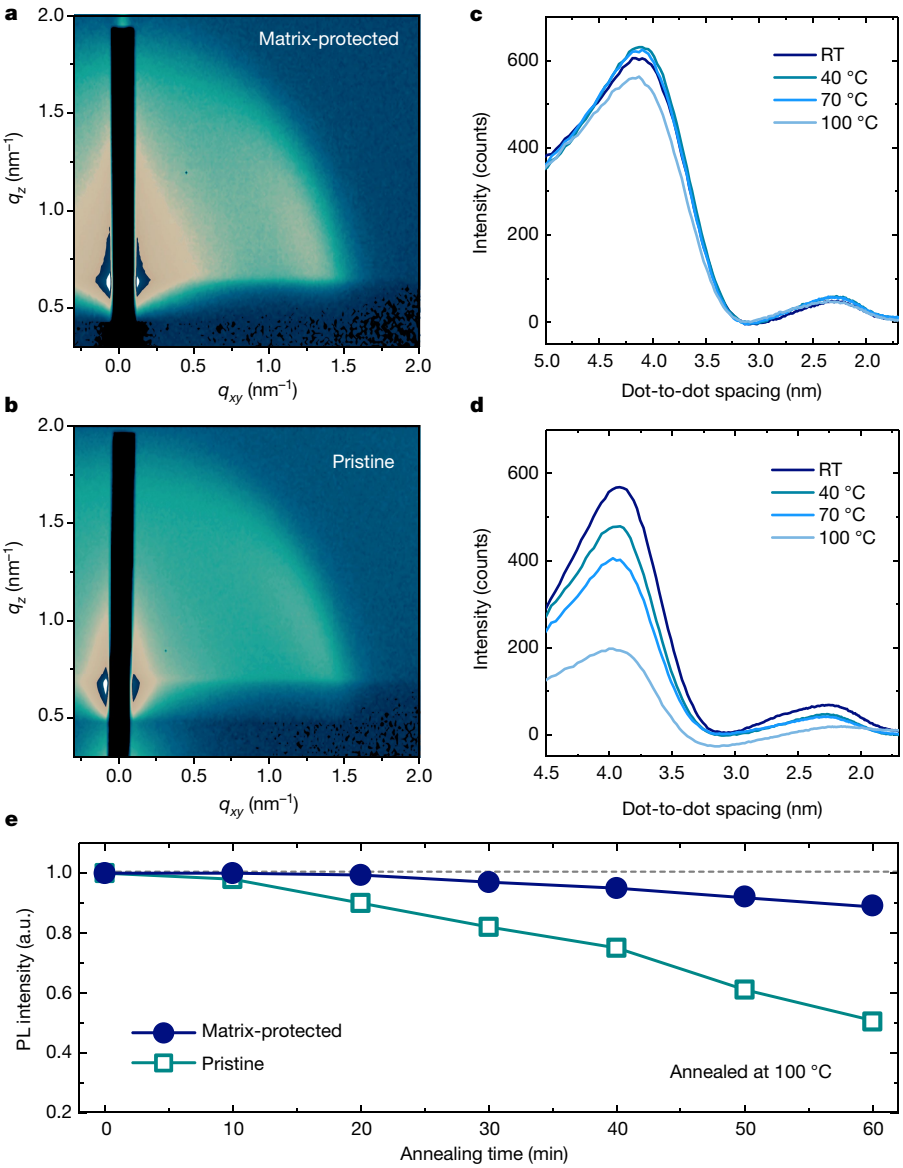

Fig. 3 | Changes in CQD packing density and uniformity at elevated temperatures. a, **b**, GISAXS two-dimensional pattern of the matrix-protected CQD film (**a**) and pristine film (**b**) measured at 70 °C. Dark colour represents lower intensity and bright colour higher intensity. The in situ GISAXS scans were taken from room temperature (RT) to 100 °C. **c**, **d**, Azimuthally integrated GISAXS intensities of the matrix-protected CQD (**c**) and pristine CQD film (**d**), showing the distribution of average dot-to-dot spacing at elevated temperatures. **e**, Changes in PL intensity for different annealing times.

In addition to improved stability, the hybrid materials also show improved optoelectronic properties. The quantum dots used in this study, which have bandgaps ranging from 1.1 eV to 1.3 eV, were predicted to experience both hole and electron confinement by the larger-bandgap $CsPbBr_xI_{3-x}$ matrix (Fig. 4a, Extended Data Fig. 7a). When the perovskite matrix is excited by light with a photon energy that exceeds its bandgap, photocarriers are generated in the perovskite and transfer from the matrix to the CQDs. This contributes to an enhanced near-infrared PL emission compared with the situation in which excitons are generated in CQDs only. At high CQD loading, the carrier transfer efficiency[24] exceeds 87% ± 3% (Fig. 4d, Extended Data Table 1). A complete quenching of the perovskite signal is also observed, consistent with efficient carrier transfer (Extended Data Fig. 7b).

The PL increases as the concentration of CQDs is reduced, and reaches its maximum in films with 7 vol% CQDs (Extended Data Fig. 7c). We studied the photoluminescence quantum efficiency (PLQE) of films having different matrix compositions to verify the effect of an epitaxially grown matrix on interface passivation (Fig. 4e). The PLQE of CQDs increases with a higher bromine ratio in the matrix and peaks at 67% bromine concentration, the value at which the lowest lattice mismatch is achieved ($\varepsilon < 0.2\%$). The lattice-matched matrix augments surface passivation of CQD solids and leads to a film PLQE of 30% ± 3% at the infrared wavelength, equivalent to the PLQE of CQD solution. The film retains its initial value of PLQE after being stored in air for one week. By contrast, the film PLQE is below 15% when the lattice mismatch is above 0.5%.

We investigated whether the inorganic matrix—with its modest conduction-band and valence-band offsets relative to the dots—could improve carrier mobility relative to prior CQD solids. Pure CQD films exhibit random close packing with a theoretical maximum volume fraction of about 64%[30]. This corresponds to about 30% of film volume that—in the absence of matrix—can be occupied by high-barrier vacuum (Fig. 4c). We posited that, when the perovskite matrix was added at a level sufficient to fill these voids substantially, this could ease transport by lowering the barrier (Fig. 4b).

We obtained carrier mobility from transient absorption spectroscopy studies and observed a doubling in mobility in the matrix-protected

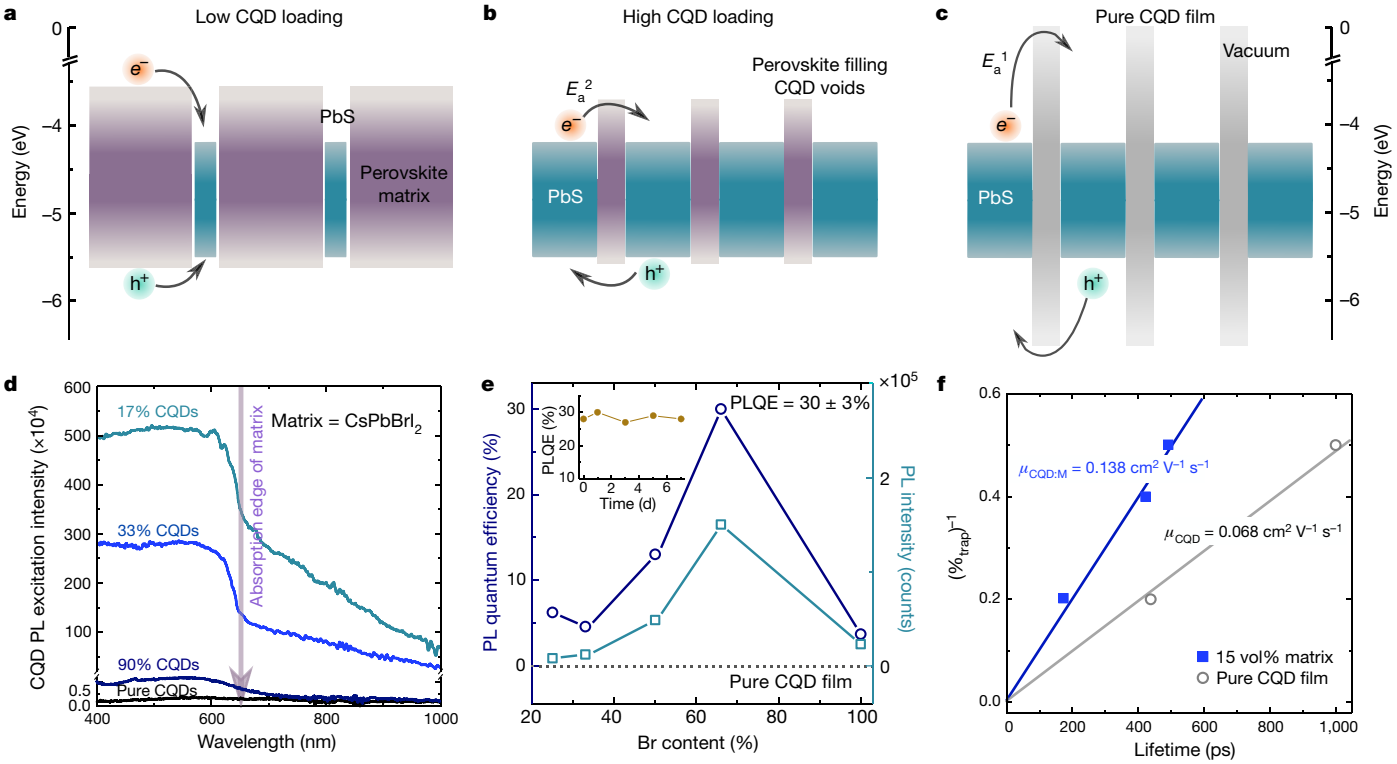

Fig. 4 | Carrier transfer and energetics within lattice-anchored CQD-in-perovskite hybrid solids. a–c, Schematics of carrier transport in the case of low CQD loading (**a**), high CQD loading (**b**) and pure CQDs (**c**). The conduction and valence bands of CQD solids reside within the bandgap of the $CsPbBr_xI_{3-x}$ matrix, forming a type-I heterojunction. At low CQD loading, the photocarriers generated in the perovskite matrix transfer to the embedded CQD solids. At high CQD loading, the carriers tunnel through the perovskite matrix by overcoming an energy barrier. **d**, PL excitation spectra of CQDs. In the perovskite absorption region, the PL excitation intensity increases as the matrix concentration increases, showing an efficient carrier transfer from the matrix to the CQDs. **e**, PL and PLQE of CQDs with different Br contents in the perovskite matrix. **f**, Carrier mobility measured by transient absorption spectroscopy. Matrix-infiltrated CQD films show a doubling in carrier mobility compared with pristine CQD films.

CQDs with 15 vol% $CsPbBr_2I$ compared with pristine CQD films (Fig. 4e, Extended Data Fig. 8).

We then pursued the realization of CQD solar cells with the best matrix-infiltrated active layer. We relied on a previously reported photovoltaic device architecture[3] (Extended Data Fig. 9a). The matrix-protected CQDs demonstrate improved photovoltaic properties relative to controls, generating higher current density and open-circuit voltage (Extended Data Fig. 9b, c). For 15 vol% $CsPbBr_2I$ matrix, the devices show a reproducibly increased performance relative to controls, and a highest PCE of 12.6%. They also exhibit enhanced photostability, retaining 95% of their initial PCE following 2 h of continuous AM1.5G illumination, unencapsulated (Extended Data Fig. 9d). The matrix-free controls, on the other hand, degrade to 70% of their initial PCE value within an hour. This result supports the contention that the lattice-matching perovskite matrix provides improved surface passivation and lowers the energy barrier for carrier hopping.

Our lattice-anchoring strategy provides solution-processed semiconductor materials with increased stability relative to either constituent phase. Incorporating CQDs into $CsPbBr_xI_{3-x}$ perovskites suppressed the formation of the undesired δ-phase configuration. This increased the lifetime of α-phase caesium lead halide perovskite, including multi-hour thermal stress at 200 °C. The epitaxially oriented perovskite matrix also provides excellent passivation to CQD surfaces, inhibiting attack from oxygen and preventing CQD fusion at elevated temperatures. In addition, the perovskite matrix lowers the energetic barrier to carrier transport, contributing to a doubling in carrier mobility. This study suggests avenues to stabilize structures such as caesium-based and formamidinium-based perovskites; to improve the thermal stability of CQDs; and to enhance the performance of solution-processed optoelectronic materials and devices.

Online content

Any methods, additional references, Nature Research reporting summaries, source data, statements of data availability and associated accession codes are available at https://doi.org/10.1038/s41586-019-1239-7.

Received: 8 August 2018; Accepted: 28 March 2019;
Published online: 22 May 2019

1. Beal, R. E. et al. Cesium lead halide perovskites with improved stability for tandem solar cells. *J. Phys. Chem. Lett.* **7**, 746–751 (2016).
2. Wang, Q. et al. Stabilizing the α-phase of $CsPbI_3$ perovskite by sulfobetaine zwitterions in one-step spin-coating films. *Joule* **1**, 371–382 (2017).
3. Liu, M. et al. Hybrid organic–inorganic inks flatten the energy landscape in colloidal quantum dot solids. *Nat. Mater.* **16**, 258–263 (2017).
4. Zhou, J., Liu, Y., Tang, J. & Tang, W. Surface ligands engineering of semiconductor quantum dots for chemosensory and biological applications. *Mater. Today* **20**, 360–376 (2017).
5. Keitel, R. C., Weidman, M. C. & Tisdale, W. A. Near-infrared photoluminescence and thermal stability of PbS nanocrystals at elevated temperatures. *J. Phys. Chem. C* **120**, 20341–20349 (2016).
6. Mitzi, D. B. Solution-processed inorganic semiconductors. *J. Mater. Chem.* **14**, 2355–2365 (2004).
7. García de Arquer, F. P. G., Armin, A., Meredith, P. & Sargent, E. H. Solution-processed semiconductors for next-generation photodetectors. *Nat. Rev. Mater.* **2**, 16100 (2017), corrigendum **2**, 17012 (2017).
8. Tan, Z.-K. et al. Bright light-emitting diodes based on organometal halide perovskite. *Nat. Nanotechnol.* **9**, 687–692 (2014).
9. Shirasaki, Y., Supran, G. J., Bawendi, M. G. & Bulović, V. Emergence of colloidal quantum-dot light-emitting technologies. *Nat. Photon.* **7**, 13–23 (2013).
10. Xu, J. et al. 2D matrix engineering for homogeneous quantum dot coupling in photovoltaic solids. *Nat. Nanotechnol.* **13**, 456–462 (2018).
11. Chuang, C.-H. M., Brown, P. R., Bulović, V. & Bawendi, M. G. Improved performance and stability in quantum dot solar cells through band alignment engineering. *Nat. Mater.* **13**, 796–801 (2014).
12. Christians, J. A. et al. Tailored interfaces of unencapsulated perovskite solar cells for >1,000 hour operational stability. *Nat. Energy* **3**, 68–74 (2018).
13. Katan, C., Mohite, A. D. & Even, J. Entropy in halide perovskites. *Nat. Mater.* **17**, 377–379 (2018).

14. Yang, W. S. et al. High-performance photovoltaic perovskite layers fabricated through intramolecular exchange. *Science* **348**, 1234–1237 (2015).
15. National Renewable Energy Laboratory. *Photovoltaic research* http://www.nrel.gov/ncpv/images/efficiency_chart.jpg.
16. Ju, M.-G. et al. Toward eco-friendly and stable perovskite materials for photovoltaics. *Joule* **2**, 1231–1241 (2018).
17. Eperon, G. E. & Ginger, D. S. B-site metal cation exchange in halide perovskites. *ACS Energy Lett.* **2**, 1190–1196 (2017).
18. Li, B. et al. Surface passivation engineering strategy to fully-inorganic cubic $CsPbI_3$ perovskites for high-performance solar cells. *Nat. Commun.* **9**, 1076 (2018).
19. Jeong, B. et al. All-inorganic $CsPbI_3$ perovskite phase-stabilized by poly(ethylene oxide) for red-light-emitting diodes. *Adv. Funct. Mater.* **28**, 1706401 (2018).
20. Xiang, S. et al. The synergistic effect of non-stoichiometry and Sb-doping on air-stable α-$CsPbI_3$ for efficient carbon-based perovskite solar cells. *Nanoscale* **10**, 9996–10004 (2018).
21. Yang, D., Li, X. & Zeng, H. Surface chemistry of all inorganic halide perovskite nanocrystals: passivation mechanism and stability. *Adv. Mater. Interfaces* **5**, 1701662 (2018).
22. Ihly, R., Tolentino, J., Liu, Y., Gibbs, M. & Law, M. The photothermal stability of PbS quantum dot solids. *ACS Nano* **5**, 8175–8186 (2011).
23. Zhang, X. et al. Inorganic $CsPbI_3$ perovskite coating on PbS quantum dot for highly efficient and stable infrared light converting solar cells. *Adv. Energy Mater.* **8**, 1702049 (2018).
24. Ning, Z. et al. Quantum-dot-in-perovskite solids. *Nature* **523**, 324–328 (2015).
25. Zhao, D., Huang, J., Qin, R., Yang, G. & Yu, J. Efficient visible–near-infrared hybrid perovskite:PbS quantum dot photodetectors fabricated using an antisolvent additive solution process. *Adv. Opt. Mater.* **6**, 1800979 (2018).
26. Yang, Z. et al. Colloidal quantum dot photovoltaics enhanced by perovskite shelling. *Nano Lett.* **15**, 7539–7543 (2015).
27. Dalven, R. Electronic structure of PbS, PbSe, and PbTe. *Solid State Phys.* **28**, 179–224 (1974).
28. Pinardi, K. et al. Critical thickness and strain relaxation in lattice mismatched II–VI semiconductor layers. *J. Appl. Phys.* **83**, 4724–4733 (1998).
29. People, R. & Bean, J. C. Calculation of critical layer thickness versus lattice mismatch for Ge_xSi_{1-x}/Si strained-layer heterostructures. *Appl. Phys. Lett.* **47**, 322–324 (1985).
30. Scott, G. D. & Kilgour, D. M. The density of random close packing of spheres. *J. Phys. D* **2**, 863–866 (1969).

Acknowledgements This publication is based in part on work supported by an award (OSR-2017-CPF-3321-03) from the King Abdullah University of Science and Technology (KAUST), by the Ontario Research Fund Research Excellence Program, by the Natural Sciences and Engineering Research Council (NSERC) of Canada and by the Compute Canada (www.computecanada.ca). This research used resources of the Advanced Photon Source, a US Department of Energy (DOE) Office of Science User Facility operated by Argonne National Laboratory under contract number DE-AC02-06CH11357, and resources of the Advanced Light Source, a DOE Office of Science User Facility under contract number DE-AC02-05CH11231. M. Liu acknowledges financial support from the Hatch Graduate Scholarship for Sustainable Energy Research. The authors thank H. Du, J. Zhang, X. Ma and C. Zou from the Tianjin University for XRD and SEM-EDX measurements. We thank E. Palmiano, L. Levina, R. Wolowiec, D. Kopilovic, M. Wei, J. Choi and Z. Huang from the University of Toronto for their help during the course of study.

Reviewer information *Nature* thanks Zheng Chen and the other anonymous reviewer(s) for their contribution to the peer review of this work.

Author contributions M.L. conceived the study and developed the hybrid materials system, fabricated solar cell devices and performed synchrotron X-ray diffraction measurements and materials stability tests. Y.C., B. Sun and B. Scheffel assisted in the fabrication of quantum dot in matrix samples. C.-S.T. performed TEM imaging. R.Q.-B. contributed to XPS measurements. A.H.P. carried out transient absorption measurements. R.M. and A.A. carried out in situ GISAXS measurements. H.T. contributed to GIWAXS measurements. G.W. contributed to photoluminescence measurements. A.P.T.K. carried out the mobility measurements. M.-J.C. performed SEM imaging and EDX analysis. O.V., F.P.G.A., S.O.K. and E.H.S. supervised the project. All authors discussed the results and assisted in the preparation of the manuscript.

Competing interests The authors declare no competing interests.

Additional information
Extended data is available for this paper at https://doi.org/10.1038/s41586-019-1239-7.
Reprints and permissions information is available at http://www.nature.com/reprints.
Correspondence and requests for materials should be addressed to E.H.S.
Publisher's note: Springer Nature remains neutral with regard to jurisdictional claims in published maps and institutional affiliations.

METHODS

CQD synthesis and ligand exchange. CQDs were synthesized and washed using previously published methods[31]. A ligand-exchange process was carried out in the solution phase in ambient air. The exchange solution was prepared by dissolving perovskite precursors (lead iodide 0.05 M, lead bromide 0.05 M, caesium iodide 0.1 M) and ammonium acetate (0.01 M) in *N*,*N*-dimethylformamide (DMF). CQD solution in octane (5–6 mg ml^{-1}) was added to the exchange solution in a 1:1 volume ratio. The mixed solution was vortexed vigorously for 3 min until CQDs completely transferred to the DMF phase. The DMF solution was then washed three times using octane. After the exchange process, CQDs were precipitated by the addition of toluene, and then separated by centrifugation. This was followed by a drying process.

Film fabrication. The amount of perovskite matrix, and thus the average dot-to-dot distance, is tuned through the ratio of CQD to perovskite. For perovskite-dominant films with less than 15 vol% CQDs, the exchanged CQDs were redispersed in 0.4 M $CsPbBr_xI_{3-x}$ perovskite precursor solution in a mixed solvent of 4:1 dimethyl sulfoxide (DMSO) to DMF. The $CsPbI_3$ matrix solution was prepared following a reported method[2]. For CQD-dominant films with CQD loading above 30 vol%, matrix solution was added first to the exchanged CQDs, resulting in a partially dispersed CQD paste. Butylamine, a solvent widely used in CQD film fabrication, was then added to increase the solubility and disperse the dots completely. The hybrid ink was deposited by spin-coating at 2,000 r.p.m. for 60 s to achieve an optimized thickness. This was followed by an annealing process to crystallize the matrix and remove solvent residues. This method can be extended to a larger scale by spray coating and blade coating.

High-energy X-ray diffraction measurements. CQD/perovskite samples were made using the abovementioned spin-coating process. High-energy X-ray diffraction experiments were conducted at the 6-ID-D beamline at Argonne National Laboratory, USA. The energy of the X-ray incident beam was 100.329 keV. The two-dimensional (2D) setup was applied for data collection with a Perkin Elmer model 1621 X-ray area detector. The results of the diffraction patterns were calculated using Fit2D software.

X-ray scattering measurements. GISAXS measurements were performed at the D1 beamline, Cornell High Energy Synchrotron Source (CHESS). The wavelength of the X-ray beam used was 1.155 Å. A wide-bandpass (1.47%) double-bounce multilayer monochromator was used. The scattering patterns were obtained at a photon-incident angle of 0.5° with respect to the sample plane. A heating stage was set up for temperature-dependent in situ studies. The GISAXS scans were taken from 40 °C to 100 °C. The annealing temperature was increased by 30 °C at a time and kept at each temperature for 20 min.

Grazing-incidence wide-angle X-ray scattering (GIWAXS) measurements were performed at beamline 7.3.3 at the Advanced Light Source, Lawrence Berkeley National Laboratory. Wavelength of the X-ray beam was 1.24 Å. The scattering patterns were obtained at a photon-incident angle of 0.25° with respect to the sample plane. Samples were scanned in a helium environment to reduce air scattering. Exposure times were 30 s. The scattering patterns were recorded using a Pilatus 2M detector at a fixed distance of 277.674 mm. Calibration of the lengths in reciprocal space was done by using silver behenate. Samples for GISAXS and GIWAXS were spin-coated on glass substrates following the same spin coating and annealing procedures as were used in film fabrication.

HRTEM and EELS measurements. HRTEM samples were prepared by spin-coating the CQDs in perovskite precursor solution onto an ultrathin-carbon film (Ted Pella 01800-F). The samples were baked at 80 °C for 20 min and stored under high vacuum overnight. The HRTEM images and EELS elemental maps were then taken on a Hitachi HF-3300 instrument with 300 kV accelerating voltage observation condition.

SEM and EDX measurements. The morphologies and elemental maps of the prepared films were investigated using SEM and EDX on a Hitachi SU8230 apparatus.

PL, PLQE and the calculation of carrier transfer efficiency. PL measurements were carried out using a Horiba Fluorolog system. Steady-state PL was acquired with a time-correlated single-photon-counting detector and a monochromatized xenon lamp excitation source. The film was placed at an incident angle of 30° away from the detector to avoid reflections of the incident beam. The PLQE is measured using an integrating sphere and calculated following a reported method[32].

The carrier transfer efficiency (η) was defined as:

$$\eta = \frac{\eta_{\text{transfer}}}{\eta_{\text{total}}}$$

where n_{transfer} is the number of charge carriers that are transferred into the CQDs from the perovskite, and n_{total} is the total number of carriers photogenerated in the perovskite. The transfer efficiency η is extracted from PLQE measurement using a previously reported method[24].

We measured the PL from CQDs in lattice-anchored matrix using two excitation wavelengths: a short wavelength that excites both CQDs and perovskite, and a long wavelength that excites only CQDs. The PL of CQDs in these two scenarios are

$$\text{PL}_{\text{CQDs,short}} = (A_{\text{CQDs,short}} + \eta A_{\text{p,short}}) \times \text{PLQE}_{\text{CQDs}} \times I_{\text{ex,short}} \quad (1)$$

$$\text{PL}_{\text{CQDs,long}} = A_{\text{CQDs,long}} + \text{PLQE}_{\text{CQDs}} \times I_{\text{ex,short}} \quad (2)$$

PL_{CQDs} and I_{ex} represent the PL yield from the CQDs (in photons per second) and the photon intensity of the excitation source (in photons per second), respectively. A_{CQDs} and A_{p} are the absorption of the CQDs and the perovskite component, respectively. From equations (1) and (2), we determine

$$\eta_{\text{total}} = \left[\left(\frac{\text{PL}_{\text{CQDs,short}} \times I_{\text{ex,long}}}{\text{PL}_{\text{CQDs,long}} \times I_{\text{ex,short}}}\right) \times A_{\text{CQDs,long}} - A_{\text{CQDs,short}}\right] \frac{1}{A_{\text{p,short}}} \quad (3)$$

The measured values of $\text{PL}_{\text{CQDs}}/I_{\text{ex}}$ and the absorption results are presented in Extended Data Table 1.

Extraction of mobility from transient absorption spectroscopy. Charge-carrier mobilities were obtained with the aid of ultrafast and nanosecond transient absorption spectroscopy[33]. The amplitude of the band-edge bleach signal in transient absorption spectroscopy is representative of the band-edge carrier population[34]. When small-bandgap carrier-acceptor CQDs were added to large-bandgap carrier-donor CQDs at given concentrations (N_t), the change in donor CQD lifetime (τ) with varying N_t of acceptor CQDs provides the diffusion coefficient (D) and mobility (μ).

$$D = \frac{d}{6\sigma(\tau/N_t^{-1})}$$

σ is the capture cross-section, which for the 3D model is assumed to be $\frac{1}{4}\pi d^2$ (ref. [35]). Population transfer can be monitored directly by tracking the decay in the donor CQD bleach signals (Extended Data Fig. 8). When N_t^{-1} is plotted against τ, the resulted slope is proportional to mobilities of carriers (Fig. 4f). The matrix-infiltrated CQD film shows a twofold improvement in carrier mobility compared to pristine CQD films.

Transient absorption spectra were recorded using a femtosecond pump–probe spectroscopy. Femtosecond laser pulses were produced by a regeneratively amplified Yb:KGW laser at a 5 kHz repetition rate (Light Conversion, Pharos). By passing a portion of the 1,030 nm fundamental through an optical parametric amplifier (Light Conversion, Orpheus), the pump pulse was generated. The second harmonic of the signal pulse was selected for 750 nm light. Both the pump pulse and probe (fundamental) were directed into an optical bench (Ultrafast, Helios), where a white-light continuum was generated by focusing the 1,030 nm fundamental through a sapphire crystal. Low excitation fluence of N=0.001 was used to avoid the Auger recombination. The time delay (time resolution ~350 fs) was adjusted by optically delaying the probe pulse, with time steps increasing exponentially. A chopper was used to block every other pump pulse. Each probe pulse was measured by a charge-coupled device after dispersion by a grating spectrograph (Ultrafast, Helios). Samples were prepared on glass substrate and translated at 1 mm s^{-1} during the measurement. Pump fluences were kept at 8 μJ cm^{-2}. Kinetic traces were fitted to the convolution of the instrument response and a sum of exponential decays. Time zero was allowed to vary with wavelength to account for the chirp of the probe.

Data availability

The data that support the findings of this study are available from the corresponding authors on reasonable request.

31. Ning, Z. et al. Air-stable n-type colloidal quantum dot solids. *Nat. Mater.* **13**, 822–828 (2014).
32. de Mello, J. C., Wittmann, H. F. & Friend, R. H. An improved experimental determination of external photoluminescence quantum efficiency. *Adv. Mater.* **9**, 230–232 (1997).
33. Proppe, A. H. et al. Picosecond charge transfer and long carrier diffusion lengths in colloidal quantum dot solids. *Nano Lett.* **18**, 7052–7059 (2018).
34. Gilmore, R. H., Lee, E. M. Y., Weidman, M. C., Willard, A. P. & Tisdale, W. A. Charge carrier hopping dynamics in homogeneously broadened PbS quantum dot solids. *Nano Lett.* **17**, 893–901 (2017).
35. Zhitomirsky, D., Voznyy, O., Hoogland, S. & Sargent, E. H. Measuring charge carrier diffusion in coupled colloidal quantum dot solids. *ACS Nano* **7**, 5282–5290 (2013).

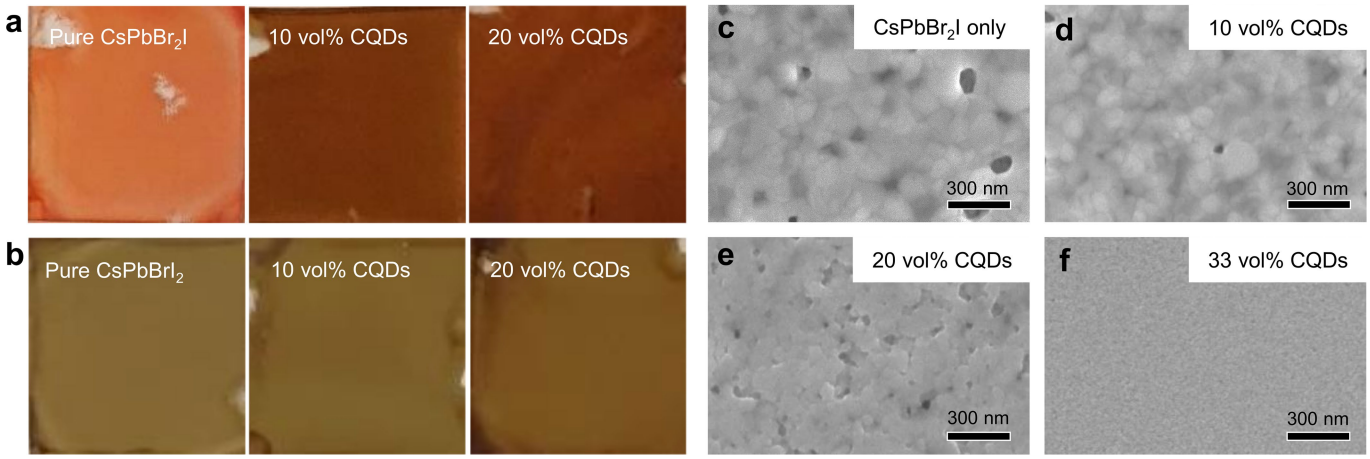

Extended Data Fig. 1 | Morphology of CQD:perovskite hybrid films. **a**, Photographs of as-prepared $CsPbBr_2I$ films with 0, 10 and 20 vol% of CQDs (from left to right). **b**, Photographs of as-prepared $CsPbBrI_2$ films with 0, 10 and 20 vol% of CQDs (from left to right). **c**–**f**, SEM images of the pure $CsPbBr_2I$ film (**c**) and CQD:$CsPbBr_2I$ hybrid films with 10 vol% (**d**), 20 vol% (**e**) and 33 vol% (**f**) CQD. At low CQD loading (10 vol%), no significant changes were observed in grain size. This argues against a main role for grain size on stability. When CQD loading is higher than 20 vol%, a smaller grain size is observed, which is consistent with the XRD peak broadening shown in Fig. 1c.

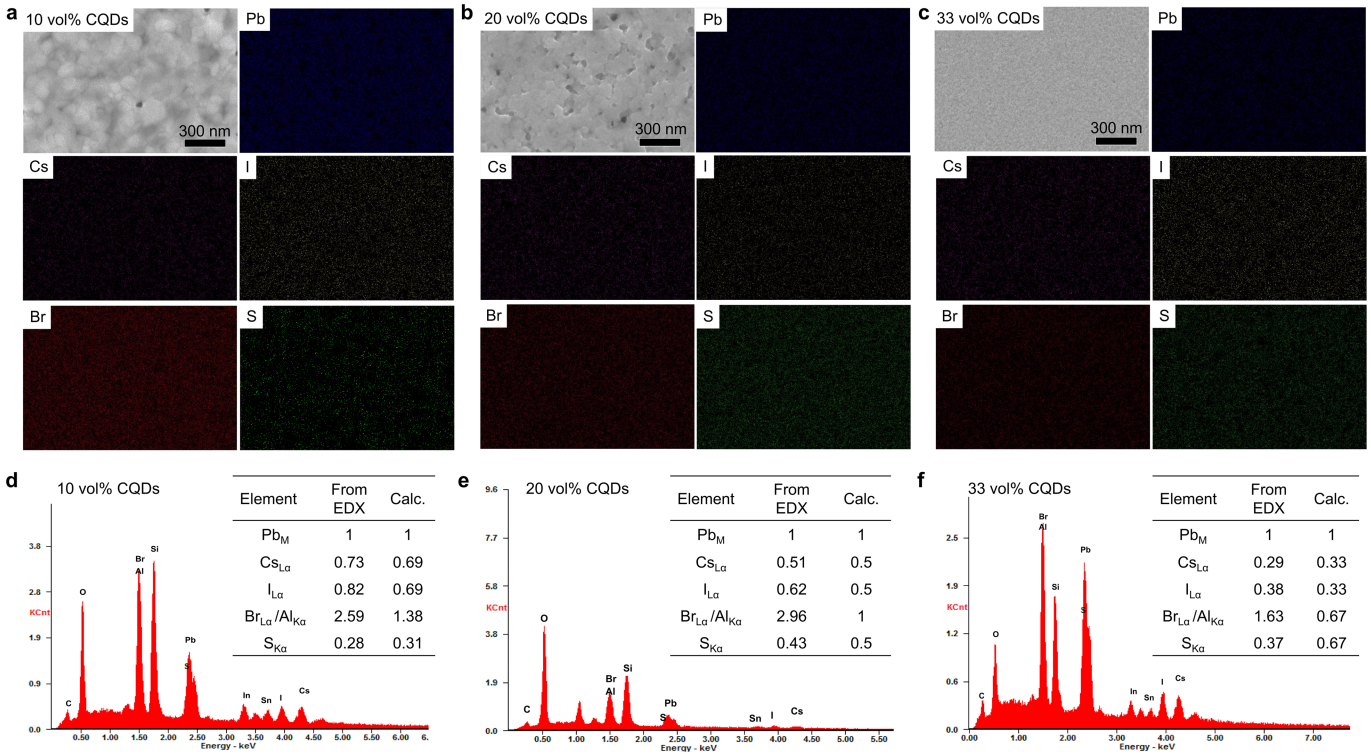

Element	From EDX	Calc.
Pb_M	1	1
$Cs_{L\alpha}$	0.73	0.69
$I_{L\alpha}$	0.82	0.69
$Br_{L\alpha}/Al_{K\alpha}$	2.59	1.38
$S_{K\alpha}$	0.28	0.31

Element	From EDX	Calc.
Pb_M	1	1
$Cs_{L\alpha}$	0.51	0.5
$I_{L\alpha}$	0.62	0.5
$Br_{L\alpha}/Al_{K\alpha}$	2.96	1
$S_{K\alpha}$	0.43	0.5

Element	From EDX	Calc.
Pb_M	1	1
$Cs_{L\alpha}$	0.29	0.33
$I_{L\alpha}$	0.38	0.33
$Br_{L\alpha}/Al_{K\alpha}$	1.63	0.67
$S_{K\alpha}$	0.37	0.67

Extended Data Fig. 2 | EDX mapping and elemental analysis of CQD:$CsPbBr_2I$ hybrid films. a–c, EDX mapping of $CsPbBr_2I$ films with 10 vol% (**a**), 20 vol% (**b**) and 33 vol% (**c**) CQDs . **d–f**, Elemental analysis of films in **a–c**, respectively. An aluminium specimen holder was used for the measurement, resulting in a strong Al signal in the EDX analysis. The energy peak of $Al_{K\alpha}$ (1.486 keV) overlaps with $Br_{L\alpha}$ (1.480 keV) in the EDX spectra. To avoid sample damage, an accelerating voltage of 10 keV was used, which is unable to detect the signal from $Br_{K\alpha}$ (11.922 keV). As a result, we cannot ascertain the elemental ratio of Br in the film. The values from the experiments and calculations are presented in the inset tables. The elemental ratios are normalized to Pb.

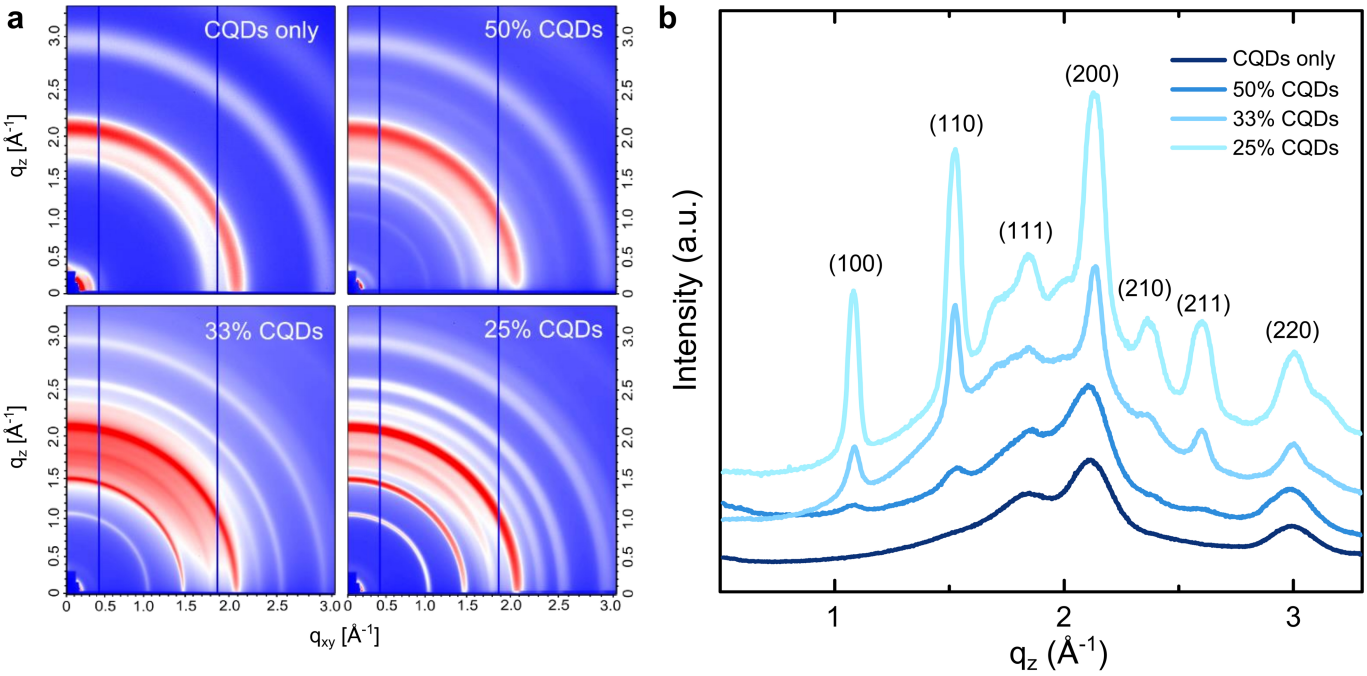

Extended Data Fig. 3 | X-ray diffraction of the CQD:CsPbBr$_2$I films. a, Two-dimensional GIWAXS patterns of CQD:CsPbBr$_2$I films. **b**, Azimuthal integrated line profile along the q_z axis.

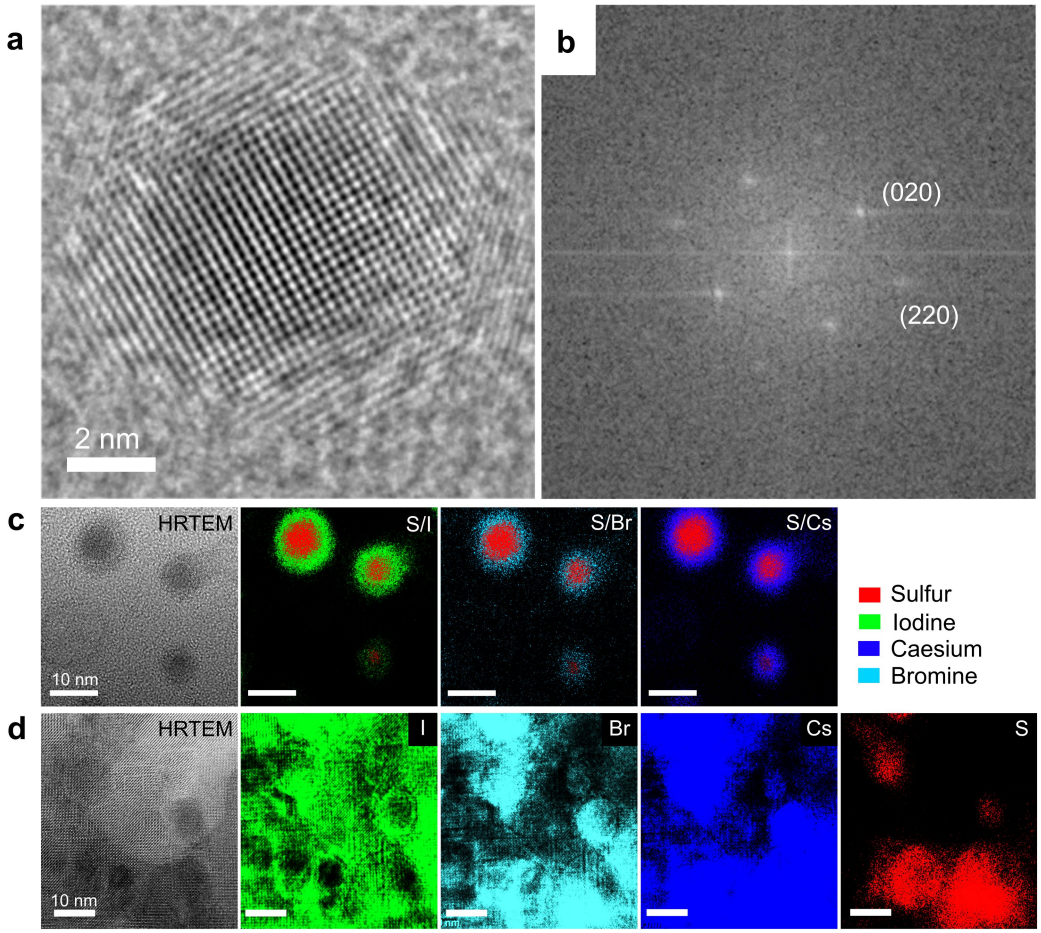

Extended Data Fig. 4 | Morphological and structural characterization of CQD:perovskite hybrid structures. a, **b**, HRTEM (**a**) and fast Fourier transform (**b**) images of PbS quantum dots with a thin $CsPbBrI_2$ perovskite shell. The shell has a lower contrast than the CQDs, as $CsPbX_3$ has a lower density than PbS. **c**, **d**, Scanning TEM images and EELS elemental mapping of a CQD/$CsPbBrI_2$ core–shell structure (**c**) and a CQD-in-$CsPbBrI_2$-matrix structure (**d**).

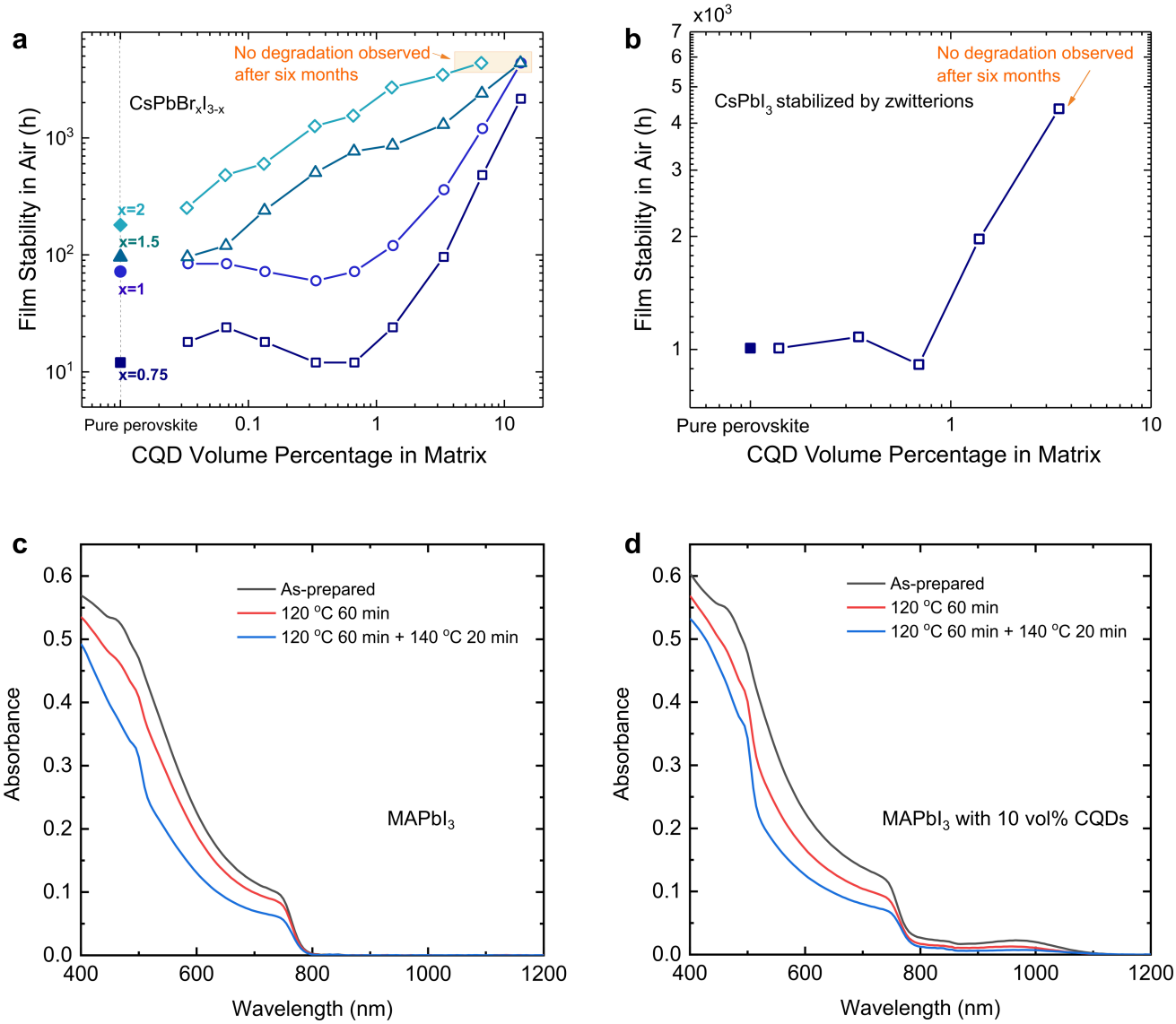

Extended Data Fig. 5 | Stability studies of lattice-anchored and control materials system. a, Stability of the lattice-anchored perovskite with mixed halides. The film stability is improved from a couple of days to several months. For Br content higher than 33%, the perovskite film could be stabilized in room ambient conditions for more than 6 months without any degradation. **b**, Stability of the lattice-anchored α-phase $CsPbI_3$. The fabrication of $CsPbI_3$ films follows a reported method (ref. [2]), which exhibits 1,000-h air stability for the pure perovskite matrix. CQDs further enhanced the stability to greater than 6 months, showing the compatibility of this strategy with previous methods. **c**, **d**, Thermal stability studies of methylammonium lead iodide ($MAPbI_3$) films with and without CQDs, as a control material. Absorption spectra of pure $MAPbI_3$ (**c**) and $MAPbI_3$ with 10 vol% CQDs (**d**) before and after annealing in ambient air. The degradation of $MAPbI_3$ perovskite arises from the volatility of organic components. The CQD:$MAPbI_3$ film does not show any improvement in thermal stability compared with pure $MAPbI_3$. The reduced and broadened excitonic peak of PbS shows an increase in CQD aggregation.

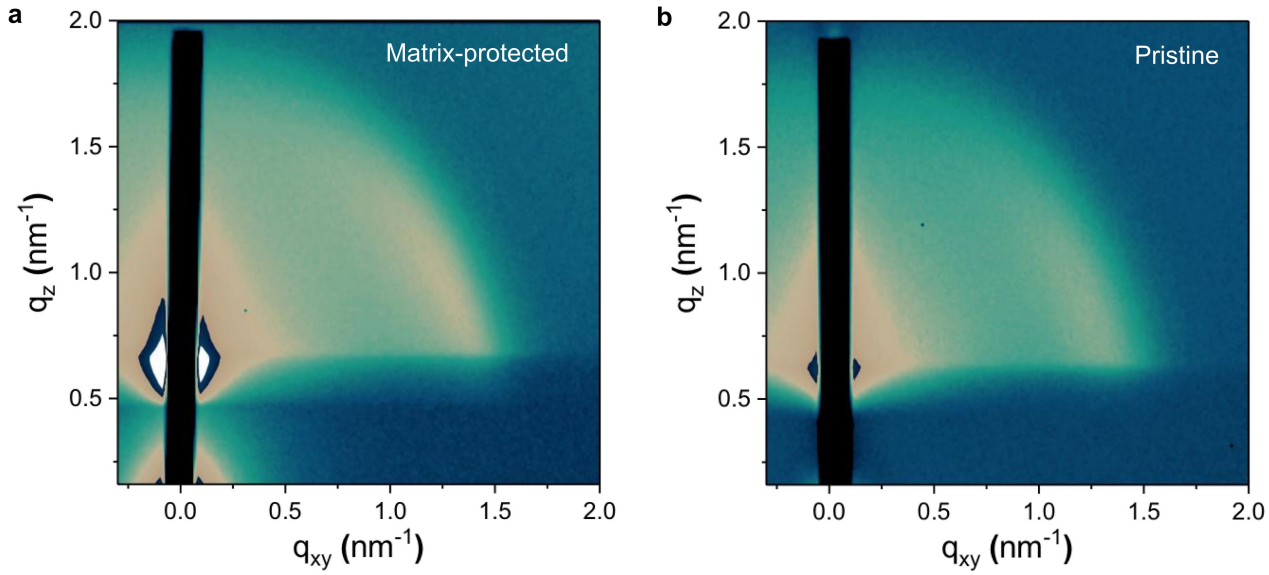

Extended Data Fig. 6 | GISAXS 2D pattern of the matrix-protected CQD films and pristine films measured at room temperature. a, Matrix-protected CQD film. **b**, Pristine film.

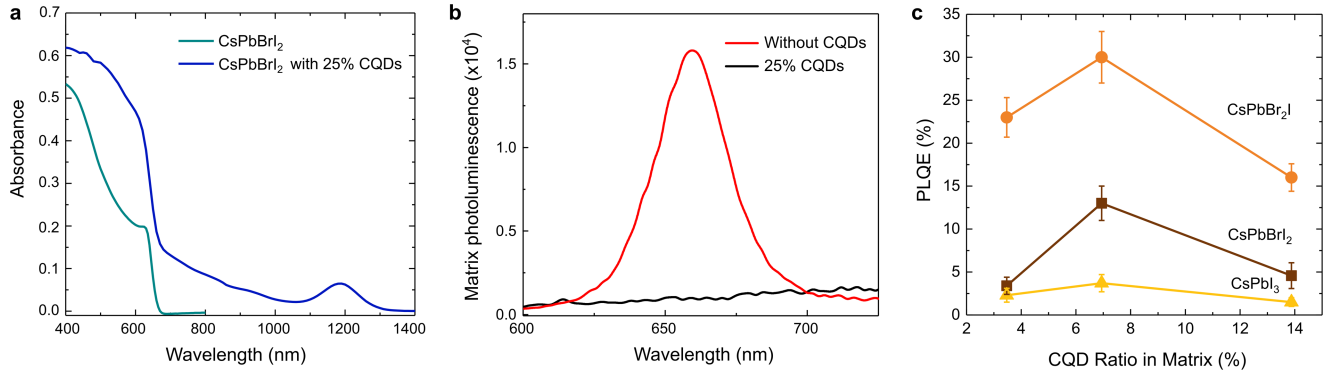

Extended Data Fig. 7 | Photophysical studies of CQD-in-matrix hybrid films. a, Absorption spectra of $CsPbBrI_2$ film with and without CQDs embedded. **b**, PL quenching at perovskite emission range. When CQDs are embedded, the PL signal from perovskite is completely quenched, showing an efficient carrier transfer from the matrix to the CQDs. **c**, PL quantum yield of CQD-in-matrix films at different CQD ratios.

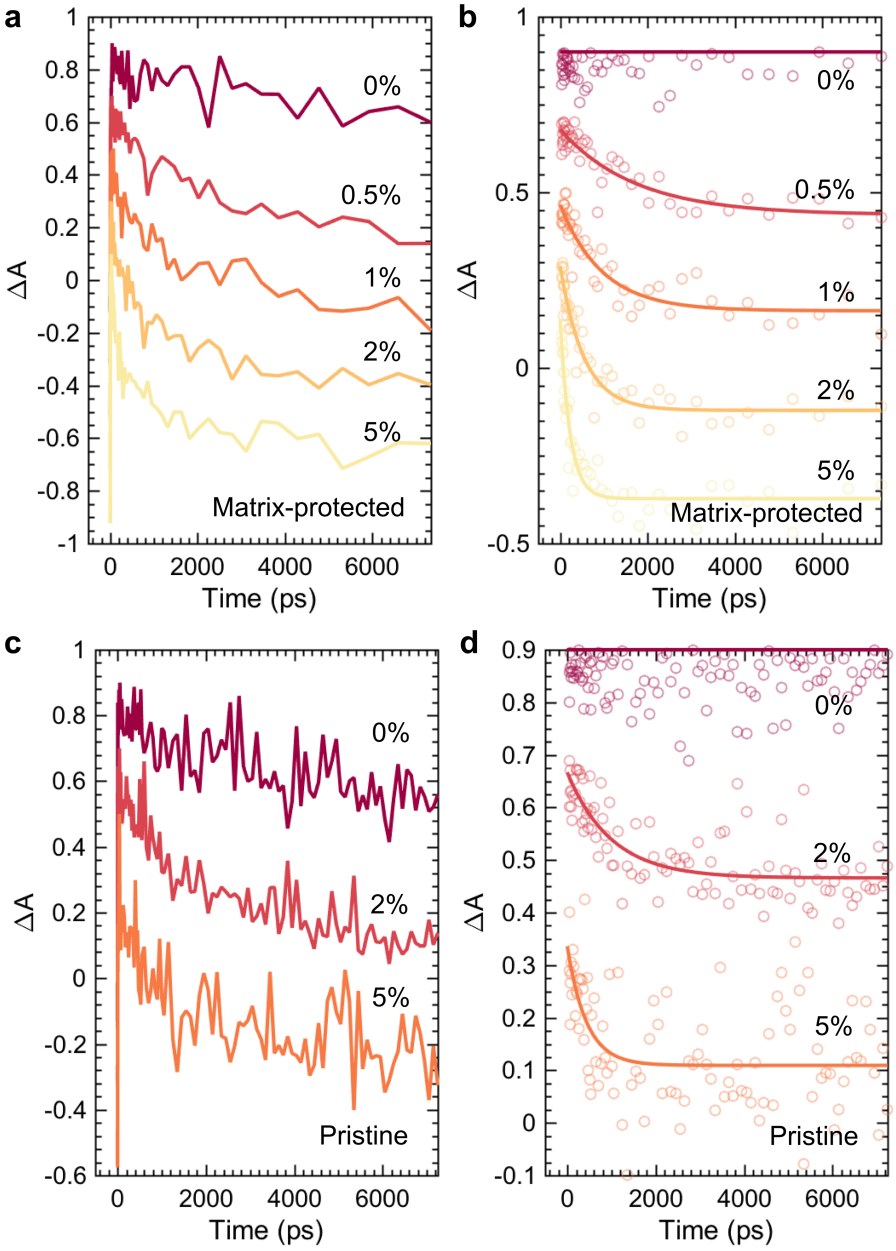

Extended Data Fig. 8 | Mobility studies of matrix-protected CQD films and pristine CQDs from the dependence of the carrier lifetime on trap percentage. a, **c**, Time traces at the exciton bleach peak of 960-nm-bandgap CQD donor films with a range of acceptor CQD concentrations, increasing from top (0%) to bottom (5%). **b**, **d**, Data with fits after subtracting Auger dynamics from the pure donor film, with fitted values for lifetime and offset. *A*, absorption.

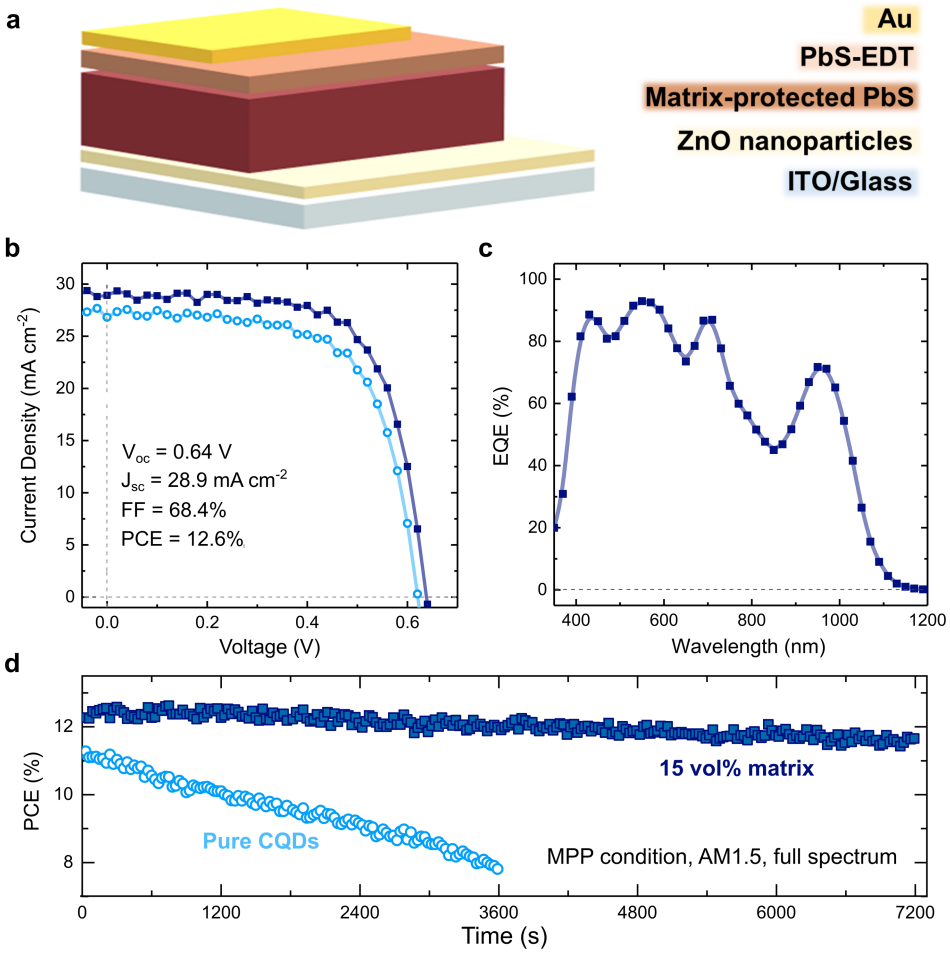

Extended Data Fig. 9 | CQD solar cell devices. a, Device architecture. **b–d**, Solar cell performance. Dark blue curves represent the matrix-infiltrated CQD samples, and the light blue curves represent the pure CQD samples. **b**, Current density versus voltage (*J–V*) curves. **c**, EQE. **d**, Stability test with continuous AM1.5G illumination unencapsulated. oc, open circuit; sc, short circuit; FF, fill factor; MPP, maximum power point.

Extended Data Table 1 | Photophysical parameters of lattice-anchored hybrid material

$PL_{CQDs,short}/I_{ex,short}$	$PL_{CQDs,long}/I_{ex,long}$	$A_{CQDs,short}$	$A_{CQDs,long}$	$A_{p,short}$
5135476	813487	0.11	0.07	0.38

PL_{CQDs} and I_{ex} represent the PL yield from the CQDs (in photons per second) and the photon intensity of the excitation source (in photons per second), respectively. A_{CQDs} and A_p is the absorption of CQDs and the perovskite component, respectively.